Progress In Electromagnetics Research, Vol. 160, 29–39, 2017

High-Resolution Grid-Independent Imaging for Terahertz 2-D Synthetic Aperture Radar with Spatial Under-Sampling

Li Ding[1, 2, 3], Xi Ding[2], Yangyang Ye[2], Sixuan Wu[2], and Yiming Zhu[1, 2, 3, *]

Abstract—For the purpose of two-dimensional (2-D) imaging in the Terahertz (THz) near field through 2-D synthetic aperture radar technology, Fourier transform (FT) is one of the most popular imaging ways. However, FT-based algorithms would encounter performance loss either when spatial sampling is under Nyquist frequency or there are off-grid scatterers in the scene of interest. Therefore, by exploiting the theory of matrix enhancement and continuous parameter estimation, we propose to use matrix enhancement and matrix pencil (MEMP) method and matched filter to deal with arbitrarily located scatterers when spatial under-sampling is adopted. Through constructing a specifically expanded matrix, the information of the scatterers involved in the small data set can be enhanced. Then, high-resolution grid-independence 2-D imaging can be achieved by the combination of MP and matched filter. Simulation results verify the effectiveness of the proposed algorithm.

1. INTRODUCTION

Terahertz (THz) benefited from its low radiation energy, strong penetration and high resolution has spurred a surge of interests into the imaging fields, especially into the security-related applications [1–6].

Currently, THz spatial two-dimensional (2-D) imaging is popularly implemented by the synthetic aperture radar (SAR) technology. Although SAR is a well-known technique trading time for space in the microwave imaging region [7, 8], many geometries of inversion problems can be seen as interesting variants of SAR, such as the transceiver array in [9] by trading cost for time. For the imaging method, Fourier transform (FT), which is widely used in the classical microwave SAR fields, is also a way of well-known imaging in the THz band [2–6]. [3] has proposed a surveillance system with a vertical linear antenna array actuated over a circular path to obtain a 360° cylindrical scan, and similarly for such a SAR with circular trajectory, [4] has provided a nonuniform FT-based algorithm to decrease the computation complexity. Operating at difference THz band, [5] has elaborated the outcomes obtained by a 2-D planar SAR with broadband sweep signals, while [6] has proposed an imaging scheme based on frequency-controlled beam scanning antenna to speed up the scene scanning. However, no matter what strategy the system is, the imaging method with respect to the derived analytical expression belongs to FT scope. Traditional FT-based methods have several drawbacks when being applied into THz fields. One of the most important factors is the shorter wavelength of THz radiation, which implies the reduced sampling interval in space. In order to utilize FT, spatial sampling should obey Nyquist theory to obtain a full set of data [3, 4]. This leads to a larger amount of data and dramatically increases the signal acquisition time. The corresponding system cost will scale up, especially when achieving a high spatial resolution performance by enlarging the synthetic aperture lengths in both x- and y-azimuth

Received 1 April 2017, Accepted 14 October 2017, Scheduled 30 October 2017

* Corresponding author: Yiming Zhu (ymzhu@usst.edu.cn).

[1] Terahertz Technology Innovation Research Institute, No. 516 JunGong Road, Shanghai 200093, China. [2] Shanghai Key Lab of Modern Optical System, University of Shanghai for Science and Technology, No. 516 JunGong Road, Shanghai 200093, China. [3] Terahertz Science Cooperative Innovation Center, Shanghai 200093, China.

dimensions. It is obviously not conducive to the application of THz imaging technology. Besides, FT has a nature of discrete parameter estimation, which is inherent to solve linear inverse problems arising from discretization on a continuum. This assumes both that the imaging scene consists of 2-D predefined grids and that all the scatterers are located exactly on these grids. Otherwise, those off-grid scatterers would severely affect the imaging performance [10, 11].

Recently, the theory of compressed sensing (CS) has attracted increased research interests to deal with the imaging problem when the data set is obtained not following Nyquist theory [12, 13]. However, CS-based reconstruction still belongs to the scope of discrete parameter estimation. Thus, it cannot avoid the off-grid phenomenon, and would lead to the well-known basis mismatch problem [10, 11]. Besides, conventional methods for continuous parameter estimation [14, 15], such as the estimating signal parameters via rotational invariance techniques (ESPRIT), and the matrix pencil (MP) method, which are free of grid dependence, would become less effective if the number of given samples is small by under-sampling.

Attentive to the aforementioned problems, we propose a high-resolution grid-independent imaging algorithm to achieve 2-D imaging for THz near field with spatial under-sampling. The discrete echo model in 2-D wavenumber domain for THz near-field imaging is firstly derived in detail. Towards the situation of under-sampling, by jointly utilizing the sparse nature of the targets and the continuous-parameter-estimation technique, the imaging method based on matrix extension and matrix pencil (MEMP) [16] and matched filter is proposed. The proposed algorithm is presented both to achieve imaging in 2-D azimuth plane for arbitrarily scatterers and to support a high-resolution performance by extracting the scatterer information through a mathematically matrix enhancement way. Simulation results illustrate that the proposed algorithm outperforms the traditional FT.

2. SIGNAL MODEL

The geometry of THz 2-D SAR imaging system in near field is shown in Fig. 1. The length of the effective observation plane in the x-direction is L_x, and that in the y-direction is L_y. The distance between the observation plane and the imaging scene is Z_0. The spatial sampling position of the transceiver along the x-dimension is denoted as x'_m, $m = 0, \ldots, M-1$, and M is the number of samples in the x-dimensional space. Similarly, y'_n, $n = 0, \ldots, N-1$ indicates the spatial sampling position along the y-dimension, and N is the number of samples in the y-dimensional space. The transmitted signal is $s(t) = e^{j2\pi ft}$ with the carrier frequency f. Assuming that there are L scatterers in the interested scene, the echo received by the transceiver at the position (x'_m, y'_n) is

$$s_r(x'_m, y'_n, t) = \sum_{l=1}^{L} \sigma_l(x_l, y_l) e^{j2\pi f\left(t - \frac{2R_l(x'_m, y'_n)}{c}\right)} \tag{1}$$

where $\sigma_l(x_l, y_l)$ and (x_l, y_l) are the complex reflection coefficient and position of the l-th scatterer, respectively; c is the light velocity; $R_l(x'_m, y'_n)$ is the path delay from the transceiver at (x'_m, y'_n) to the l-th scatterer and is of the form as

$$R_l\left(x'_m, y'_n\right) = \sqrt{\left(x_l - x'_m\right)^2 + \left(y_l - y'_n\right)^2 + Z_0^2} \tag{2}$$

After the quadrature down-conversion by $e^{-j2\pi ft}$, the echo signal in Eq. (1) can be expressed as

$$s_r(x'_m, y'_n) = \sum_{l=1}^{L} \sigma_l(x_l, y_l) e^{-j2\pi f \frac{2R_l(x'_m, y'_n)}{c}} \tag{3}$$

With respect to the spherical wave inherently involved in the exponential term in Eq. (3) for THz near field, the alternative of Eq. (3) can be obtained by a superposition of plane-wave components and is

$$s_r(x'_m, y'_n) = \sum_{l=1}^{L} \sigma_l(x_l, y_l) \left\{ \sum_{k_{x'}(m)} \sum_{k_{y'}(n)} e^{-jk_{x'}(m)(x_l - x'_m) - jk_{y'}(n)(y_l - y'_n) + jk_{z'}(m,n)Z_0} \right\} \tag{4}$$

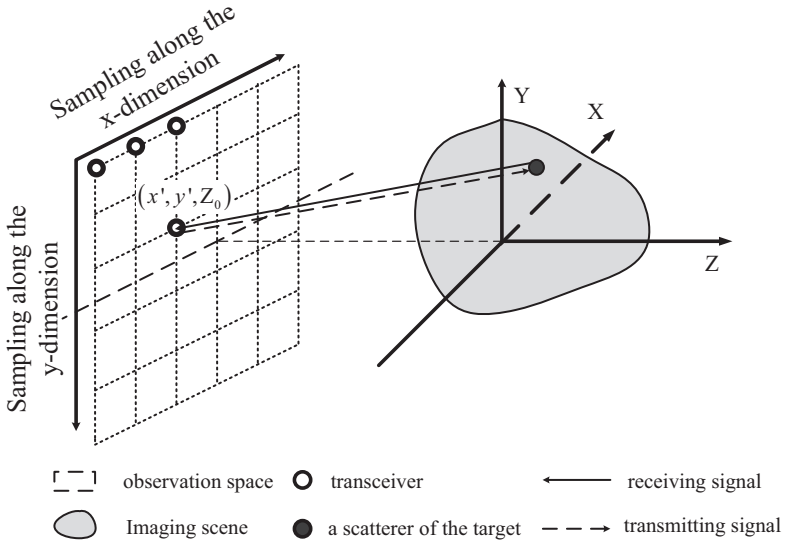

Figure 1. Terahertz 2-D SAR imaging.

where $k_{x'}(m)$ and $k_{y'}(n)$ correspond to the x- and y-dimensional wavenumber components, respectively, $k_{z'}(m,n) = \sqrt{k^2 - k_{x'}^2(m) - k_{y'}^2(n)}$, and $k = 2\pi f/c$ represents the wavenumber. It is obvious to rewrite Eq. (4) into a more enlightening way as

$$s_r\left(k_{x'}(m), k_{y'}(n)\right) = \mathrm{FT}_{2D}\left\{s_r\left(x'_m, y'_n\right)\right\} e^{-jk_{z'}(m,n)Z_0} = \mathrm{FT}_{2D}\left\{\sigma_l(x_l, y_l)\right\} \tag{5}$$

where $\mathrm{FT}_{2D}\{\cdot\}$ indicates the 2-D Fourier transform (FT).

Apparently, Eq. (5) reveals that the wavenumber-domain echo $s_r(k_{x'}(m), k_{y'}(n))$ and the reflectivity of the scatterer $\sigma_l(x_l, y_l)$ obey Fourier transform, which is the basis for analyzing the inversion performance in the wavenumber domain. At present, if the spatial sampling $(x'_m, y'_n$ in the observation plane satisfies Nyquist theory, it is clear from Eq. (5) that the reflectivity $\sigma_l(x_l, y_l)$ can be straightforwardly obtained through the inverse FT of $s_r(k_{x'}(m), k_{y'}(n))$. That is, the 2-D image reconstruction takes the form as

$$\sigma_l(x_l, y_l) = \mathrm{FT}_{2D}^{-1}\left\{\mathrm{FT}_{2D}\left\{s_r\left(x'_m, y'_n\right)\right\} e^{-jk_z(m,n)Z_0}\right\} \tag{6}$$

where $\mathrm{FT}_{2D}^{-1}\{\cdot\}$ indicates the 2-D inverse Fourier transform.

It is notable from Eq. (6) that in the THz band, the shorter wavelength, compared with the traditional microwave, renders the dramatically increased amount of data set if applying the Nyquist theory for the FT-based performance consideration. This implies the corresponding increased acquisition time and system complexity. Hence, a more appealing way to break the limitation of Nyquist law is to adopt the under-sampling scheme. However, traditional FT-based imaging gradually loses its advantages for the current cases. Although the recently arising CS theory refers to one of the most popular techniques to deal with this under-determined linear inversion problem, its grid dependence on discrete bases, which is the same as FT, makes performance loss as well. Therefore, concerning the problems of grid-independence and under-sampling in practice, it is meaningful to propose a more general imaging approach for 2-D SAR in THz near field.

3. ALGORITHM IMPLEMENTATION

Considering both the under-sampling over the 2-D observation plane and the grid independence, we take the advantage of matrix enhancement and matrix pencil (MEMP) method to make continuous parameter estimation when given a small data set. Benefited from the enhanced matrix from the samples, the proposed algorithm can obtain more information about the scatterers than the original data set shows,

so it can improve the 2-D azimuth dimension resolution without increasing the complexity of the imaging system.

Based on Equations (4) and (5), the echo signal can be expressed as

$$s_r\left(k_{x'}\left(m\right),k_{y'}\left(n\right)\right)=\sum_{l=1}^{L}\sigma_l(x_l,y_l)e^{-jk_{x'}(m)x_l-jk_{y'}(n)y_l} \tag{7}$$

In general, under the assumption that the field of view spanned by the aperture length is smaller than that of the adopted antenna itself, the wavenumber sampling $(k_{x'}(m),k_{y'}(n))$ can be assumed to meet with the following uniform relationship

$$k_{x'}\left(m\right)=\Delta k_x m,\quad k_{y'}\left(n\right)=\Delta k_y n \tag{8}$$

where Δk_x and Δk_y are the sampling intervals of x- and y-dimensional wavenumber domains, respectively, and will be approximately computed as

$$\Delta k_x=\frac{2k\frac{L_x}{\sqrt{(L_x/2)^2+Z_0^2}}}{M},\quad \Delta k_y=\frac{2k\frac{L_y}{\sqrt{(L_y/2)^2+Z_0^2}}}{N} \tag{9}$$

where it should be noted that if the non-uniformity of (k_x,k_y) over 2-D wavenumber domain cannot be ignored, the effectiveness of Eq. (9) will be guaranteed as well by inserting an additional interpolation step in advance.

By setting $q_{x,l}=e^{-j\Delta k_x x_l}$ and $q_{y,l}=e^{-j\Delta k_y y_l}$ for simplicity, Eq. (7) can also be written as

$$s_r\left(k_{x'}\left(m\right),k_{y'}\left(n\right)\right)=\sum_{l=1}^{L}\sigma_l(x_l,y_l)q_{x,l}^m q_{y,l}^n \tag{10}$$

Based on the model in Eq. (10), the detailed method of imaging by the combination of MEMP and matched filter is described in the following steps:

- ***Step 1***: Enhanced Matrix Construction

  An enhanced matrix is used for 2-D frequency estimation by partitioning and stacking as follows:

$$\mathbf{H}_e=\begin{bmatrix}\mathbf{H}_0 & \dots & \mathbf{H}_{M-K}\\ \dots & \ddots & \dots\\ \mathbf{H}_{K-1} & \vdots & \mathbf{H}_{M-1}\end{bmatrix} \tag{11}$$

where

$$\mathbf{H}_m=\begin{bmatrix}s_r\left(k_{x'}\left(m\right),k_{y'}\left(0\right)\right) & \dots & s_r\left(k_{x'}\left(m\right),k_{y'}\left(N-I\right)\right)\\ \vdots & \ddots & \vdots\\ s_r\left(k_{x'}\left(m\right),k_{y'}\left(I-1\right)\right) & \dots & s_r\left(k_{x'}\left(m\right),k_{y'}\left(N-1\right)\right)\end{bmatrix} \tag{12}$$

$\mathbf{H}_e$ is an Hankel block matrix, and $\mathbf{H}_m$ is an Hankel matrix, $m=0,1,\dots,M-1$. Each column of $\mathbf{H}_m$ is a windowed segment of the sequence $\{s_r(k_{x'}(m),k_{y'}(0)),s_r(k_{x'}(m),k_{y'}(1)),\dots,s_r(k_{x'}(m),k_{y'}(N-1))\}$ with the window length I, and $I\geq L$. Each column of $\mathbf{H}_e$ is a windowed segment of the matrix sequence $\{\mathbf{H}_0,\mathbf{H}_1,\dots,\mathbf{H}_{M-1}\}$ with the window length K, and $K\geq I$. The expanded matrix $\mathbf{H}_e$ can obtain more information about the scatterers, and it is beneficial to the improvement of imaging quality.

- ***Step 2***: 2-D Poles Estimation

  According to the position information of the scatterers involved in $q_{x,l}$ and $q_{y,l}$, we can know from Eq. (10) that the 2-D position of the scatterers will be estimated through extracting out the 2-D poles of Eq. (10). Therefore, the matrix $\mathbf{H}_e$ can be decomposed as follows

$$\mathbf{H}_e=\mathbf{U}_s\mathbf{\Sigma}_s\mathbf{V}_s^H+\mathbf{U}_n\mathbf{\Sigma}_n\mathbf{V}_n^H \tag{13}$$

where $\mathbf{U}_s$, $\mathbf{\Sigma}_s$ and $\mathbf{V}_s$ contain L major components, and $\mathbf{U}_n$, $\mathbf{\Sigma}_n$ and $\mathbf{V}_n$ contain the remaining non-major components. The superscript H denotes the complex conjugate transpose.

Let $\mathbf{U}_{s1}$ and $\mathbf{U}_{s2}$ be

$$\mathbf{U}_{s1} = \mathbf{U}_s(1 : KL - L, :) \tag{14}$$

$$\mathbf{U}_{s2} = \mathbf{U}_s(L + 1 : end, :) \tag{15}$$

According to the theory of MP, the x-dimensional poles (i.e., $\{q_{x,l}; l = 1, 2, \ldots, L\}$) can be obtained by computing the generalized eigenvalues of $\mathbf{U}_{s2} - \lambda\mathbf{U}_{s1}$. We set the outputs as $\{\hat{q}_{x,l_x}; l_x = 1, 2, \ldots, L\}$.

Furthermore, we define

$$\mathbf{U}_{sp} = \mathbf{P} \cdot \mathbf{U}_s \tag{16}$$

where P is a permutation matrix and is of the form as

$$\mathbf{P} = \begin{bmatrix} \mathbf{p}^T(1) \\ \mathbf{p}^T(1+I) \\ \vdots \\ \mathbf{p}^T(1+(K-1)I) \\ \vdots \\ \mathbf{p}^T(I) \\ \mathbf{p}^T(I+I) \\ \vdots \\ \mathbf{p}^T(I+(K-1)I) \end{bmatrix} \tag{17}$$

where $\mathbf{p}(i + jI)$ is a $KI \times 1$ vector, and except for the i-th element of value of 1, all the elements of $\mathbf{p}(i + jI)$ are zero, $i = 1, 2, \ldots, I$, $j = 0, 1, \ldots, K - 1$. To extract the poles of $\{q_{y,l}\}$, in a similar way, we form $\mathbf{U}_{sp1}$ and $\mathbf{U}_{sp2}$ from $\mathbf{U}_{sp}$ as

$$\mathbf{U}_{sp1} = \mathbf{U}_{sp}(1 : KL - L, :) \tag{18}$$

$$\mathbf{U}_{sp2} = \mathbf{U}_{sp}(L + 1 : end, :) \tag{19}$$

Then, the generalized eigenvalues of $\mathbf{U}_{s2p} - \lambda\mathbf{U}_{s1p}$ can be computed as $\{\hat{q}_{y,l_y}; l_y = 1, 2, \ldots, L\}$.

- ***Step 3***: Scatterer Position Estimation

  The x- and y-dimensional positions of the scatterer can be calculated as follows

$$\hat{x}_{l_x} = \frac{-\mathrm{Im}(\log(\hat{q}_{x,l_x}))}{\Delta k_x} \tag{20}$$

$$\hat{y}_{l_y} = \frac{-\mathrm{Im}(\log(\hat{q}_{y,l_y}))}{\Delta k_y} \tag{21}$$

- ***Step 4***: Pairing

  Although now two sets of poles, i.e., $\{\hat{q}_{x,l_x}; l_x = 1, \ldots, L\}$ and $\{\hat{q}_{y,l_y}; l_y = 1, \ldots, L\}$ have been estimated, the order in each set is still unknown. It means that the pair of $(\hat{x}_{l_x}, \hat{y}_{l_y})$ as $l_x = l_y$ is not necessarily pointing to the estimation of (x_l, y_l) of the l-th scatterer. To obtain the correct but not necessarily ordered pairs $\{(\hat{x}_l, \hat{y}_l); l = 1, \ldots, L\}$, we need to pair the two sets $\{\hat{x}_{l_x}; l_x = 1, \ldots, L\}$ and $\{\hat{y}_{l_y}; l_y = 1, \ldots, L\}$.

  For $i = 1, 2, \ldots, L$, maximizing the function shown in Eq. (22) with respect to j will yield the correct pairs $\{(\hat{x}_l, \hat{y}_l); l = 1, \ldots, L\}$ [14].

$$J_s(i, j) = \sum_{t=1}^{L} \left\| \mathbf{u}_t^H \mathbf{e}_L(\hat{q}_{x,i}, \hat{q}_{y,j}) \right\|^2 \tag{22}$$

  where $\{\mathbf{u}_t, t = 1, 2, \ldots, L\}$ express the L principal eigenvectors of $\mathbf{U}_s$, $\mathbf{e}_L(\hat{q}_{x,i}, \hat{q}_{y,j}) = \hat{\mathbf{q}}_{x,i} \otimes \hat{\mathbf{q}}_{y,j}$, and $\hat{\mathbf{q}}_{x,i} = [1, \hat{q}_{x,i}, \ldots, \hat{q}_{x,i}^{K-1}]^T$, $\hat{\mathbf{q}}_{y,j} = [1, \hat{q}_{y,j}, \ldots, \hat{q}_{y,j}^{I-1}]^T$ and $i, j = 1, \ldots, L$.

- ***Step 5***: Complex Coefficients Recovery

By bringing the estimated $(\hat{x}_l, \hat{y}_l)$ from step 4 into the echo model in Eq. (7), all the samples of $\{s_r(k_{x'}(m), k_{y'}(n)),\ m = 0, 1, \ldots, M-1,\ n = 0, 1, \ldots, N-1\}$ collected over the 2-D observation plane can be stacked as

$$\mathbf{S} = \mathbf{F}_x \boldsymbol{\sigma} \mathbf{F}_y^T \tag{23}$$

where $\mathbf{S}$, $\mathbf{F}_x$, $\mathbf{F}_y$ and $\boldsymbol{\sigma}$ denote the 2-D echo matrix, observation matrix in x-dimension, observation matrix in y-dimension and the scattering matrix, respectively. Specifically, they are

$$\mathbf{S} = \begin{bmatrix} s_r\left(k_{x'}(1), k_{y'}(1)\right) & \cdots & s_r\left(k_{x'}(1), k_{y'}(N)\right) \\ \vdots & \ddots & \vdots \\ s_r\left(k_{x'}(M), k_{y'}(1)\right) & \cdots & s_r\left(k_{x'}(M), k_{y'}(N)\right) \end{bmatrix}$$

$$\mathbf{F}_x = \begin{bmatrix} e^{-jk_{x'}(1)\hat{x}_1} & \cdots & e^{-jk_{x'}(1)\hat{x}_L} \\ \vdots & \ddots & \vdots \\ e^{-jk_{x'}(M)\hat{x}_1} & \cdots & e^{-jk_{x'}(M)\hat{x}_L} \end{bmatrix}$$

$$\mathbf{F}_y = \begin{bmatrix} e^{-jk_{y'}(1)\hat{y}_1} & \cdots & e^{-jk_{y'}(1)\hat{y}_L} \\ \vdots & \ddots & \vdots \\ e^{-jk_{y'}(N)\hat{y}_1} & \cdots & e^{-jk_{y'}(N)\hat{y}_L} \end{bmatrix}$$

$$\boldsymbol{\sigma} = \begin{bmatrix} \sigma_1(x_1, y_1) & \cdots & 0 \\ \vdots & \ddots & \vdots \\ 0 & \cdots & \sigma_L(x_L, y_L) \end{bmatrix}$$

thus, the complex reflectivity can be solved through a two-step matched filter,

$$\hat{\boldsymbol{\sigma}} = \left(\mathbf{F}_x^H \mathbf{F}_x\right)^{-1} \mathbf{F}_x^H \mathbf{S} \mathbf{F}_y^* \left(\mathbf{F}_y^T \mathbf{F}_y^*\right)^{-1} \tag{24}$$

4. SIMULATION

Here, we take the traditional FT-based algorithm as a comparison. The parameters of the considered THz 2-D SAR are set as follows. The lengths of the effective observation plane in the x-direction and y-direction are $L_x = 0.0803\,\mathrm{m}$ and $L_y = 0.0803\,\mathrm{m}$, respectively. The distance between the observation plane and the imaging scene is $|Z_0| = 0.5\,\mathrm{m}$. The center frequency of the transmitted signal is $f = 183\,\mathrm{GHz}$, and the wavelength is $\lambda = 1.64\,\mathrm{mm}$, such that both the spatial intervals in x- and y-dimensions are $\lambda/2 = 0.82\,\mathrm{mm}$ according to Nyquist theory [17]. However, we take the under-sampling, and the spatial interval in both the dimensions is set as 1.64 mm. Therefore, the numbers of sampling points along the x-dimension and y-dimension of the transceiver are $M = 50$ and $N = 50$, respectively. Let ρ_x and ρ_y denote the limit resolution of x-dimension and y-dimension, respectively. According to the parameters given above, ρ_x can be calculated as $\rho_x = \frac{\mathrm{c}}{4f}\frac{(L_x/2)^2 + Z_0^2}{(L_x/2)^2} = 5.1\,\mathrm{mm}$ [18], and similarly, $\rho_y = 5.1\,\mathrm{mm}$. The error of estimation is computed as

$$Error = \frac{1}{L}\sum_{l=1}^{L} \frac{\|\hat{\mathbf{r}}_l - \mathbf{r}_l\|_2}{\|\mathbf{r}_l\|_2}$$

where $\hat{\mathbf{r}}_\mathbf{l} = (\hat{x}_l, \hat{y}_l)^T$ and $\mathbf{r}_l = (x_l, y_l)^T$. To avoid the effect caused by the mainlobe of FT, its estimation error is calculated by picking up its L largest peaks.

By arbitrarily choosing 3 scatterers with the constraint that $|x_1 - x_2| = \rho_x, |y_2 - y_3| = \rho_y$, as shown in Fig. 2(a), Fig. 2 validates the resolution capability of the proposed algorithm. The comparison between Fig. 2(a) and Fig. 2(b) represents the failure by FT-based method and the effectiveness of the proposed approach, where the targets estimated by FT in Fig. 2(a) are unseparated, and thus the error is referred to infinity, denoted as Inf.

Furthermore, we can see from Fig. 3(a) and Fig. 3(b) that the FT-based algorithm can resolve different scatterers as the distance between any two of the scatterers increases to beyond multiple times of resolution, but is of a worse estimation performance even regardless of the mainlobe effect.

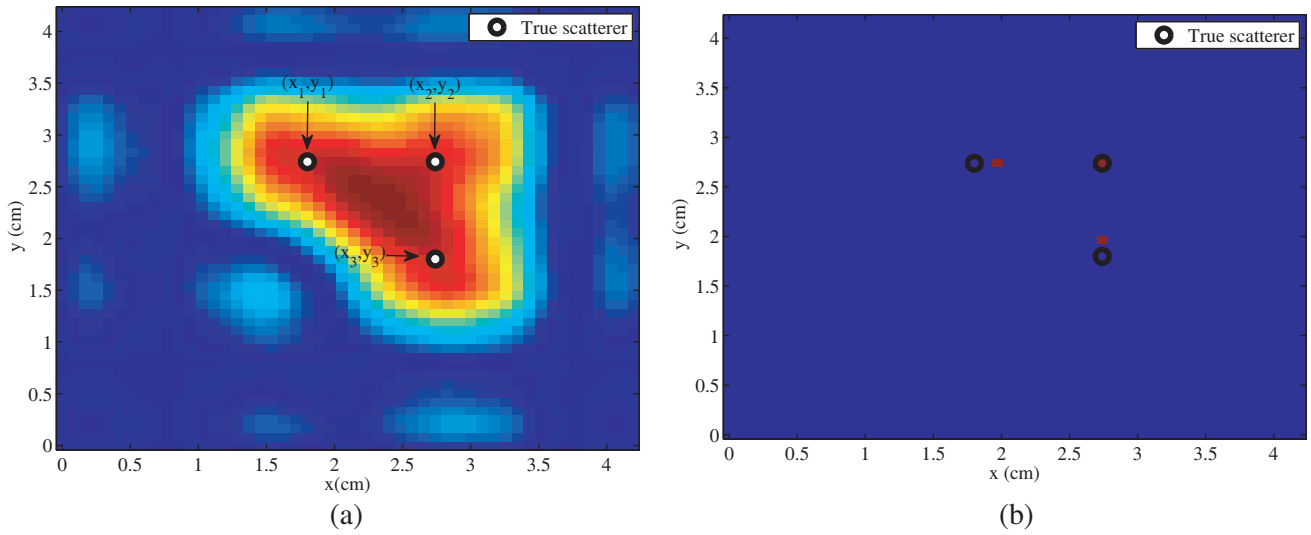

Figure 2. Under-sampling imaging comparison with $|x_1 - x_2| = \rho_x$ and $|y_2 - y_3| = \rho_y$: (a) FT (Error Inf), (b) proposed algorithm (Error 0.0384).

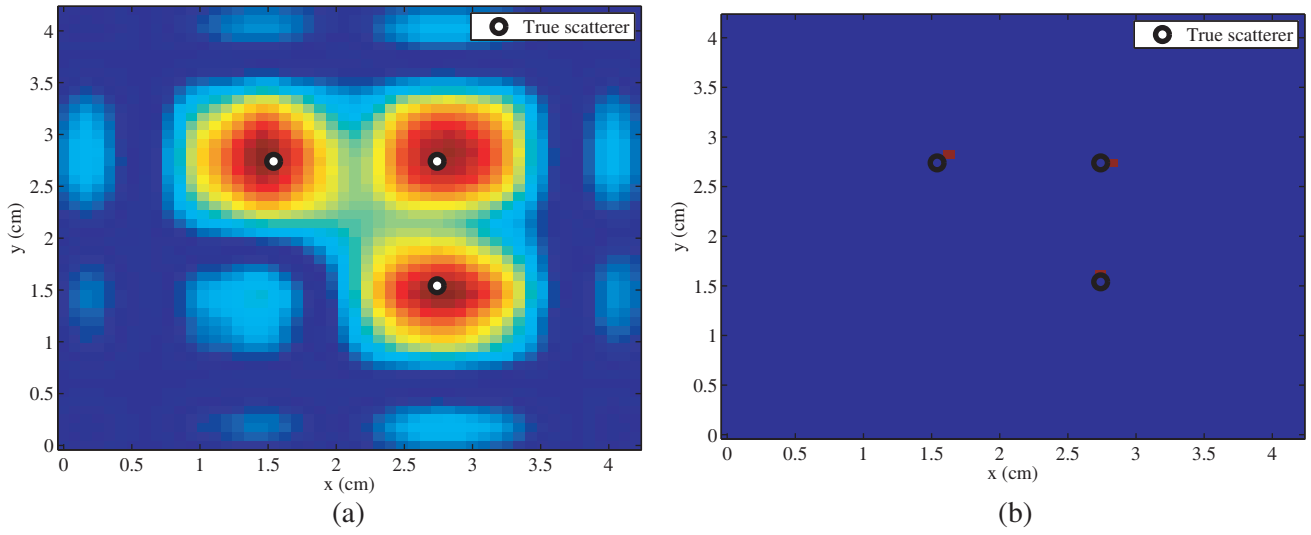

Figure 3. Under-sampling imaging comparison with $|x_1 - x_2| > 2\rho_x$ and $|y_2 - y_3| > 2\rho_y$: (a) FT (Error 0.0363), (b) proposed algorithm (Error 0.0237).

For the case of multiple scatterers, Fig. 4 shows that even compared to FT of the full data set, the proposed algorithm for under-sampling case has a pleasant reconstruction and outperforms the FT-based algorithm especially in the light of focusing performance and the estimation error.

Furthermore, the imaging performances of orthogonal matching pursuit (OMP) and our proposed algorithm are compared, where OMP is a popular algorithm in the CS field. It is well known that the grid-dependence problem limits the performance of CS-relevant algorithms. Therefore, by arbitrarily choosing 5 scatterers in the scene, the imaging results by the two algorithms are shown in Fig. 5(a) and Fig. 5(b), respectively. Obviously, Fig. 5 demonstrates that our proposed approach can provide better imaging than OMP when off-the-grid scatterers exist.

Then the performance of the proposed algorithm with respect to varying number of samples as well as the resolving capability versus the varying x-dimensional distance between two scatterers is examined, shown in Fig. 6. Inferred from Fig. 3, two scatterers with the spacing greater than multiple

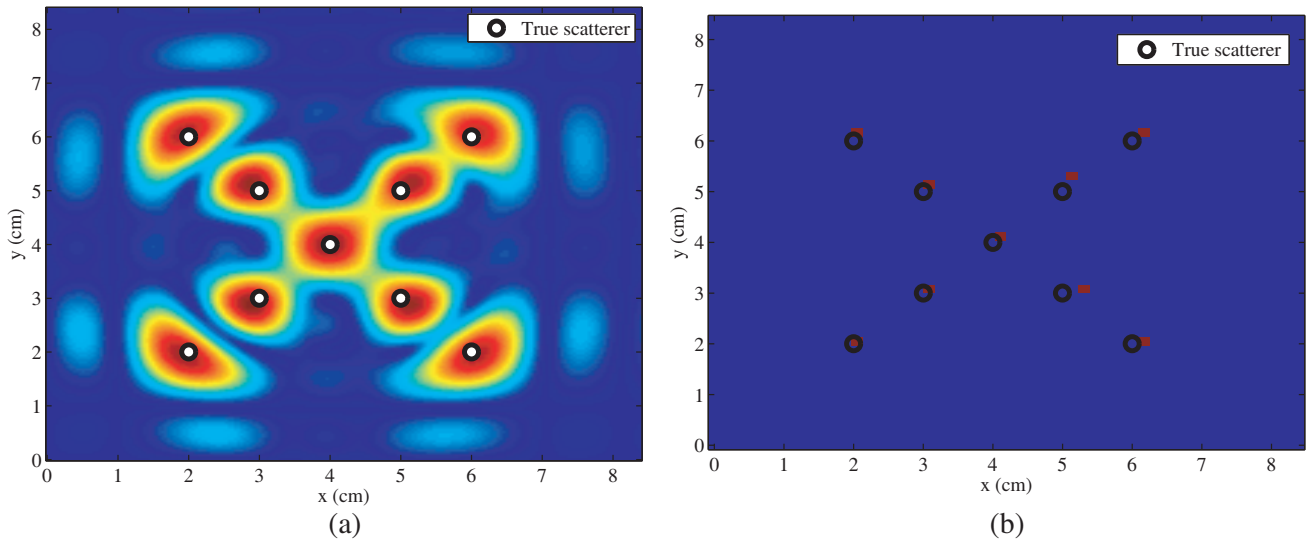

Figure 4. Imaging comparison: (a) FT (full data set, Error 0.0319), (b) proposed algorithm (undersampling, (Error 0.0211).

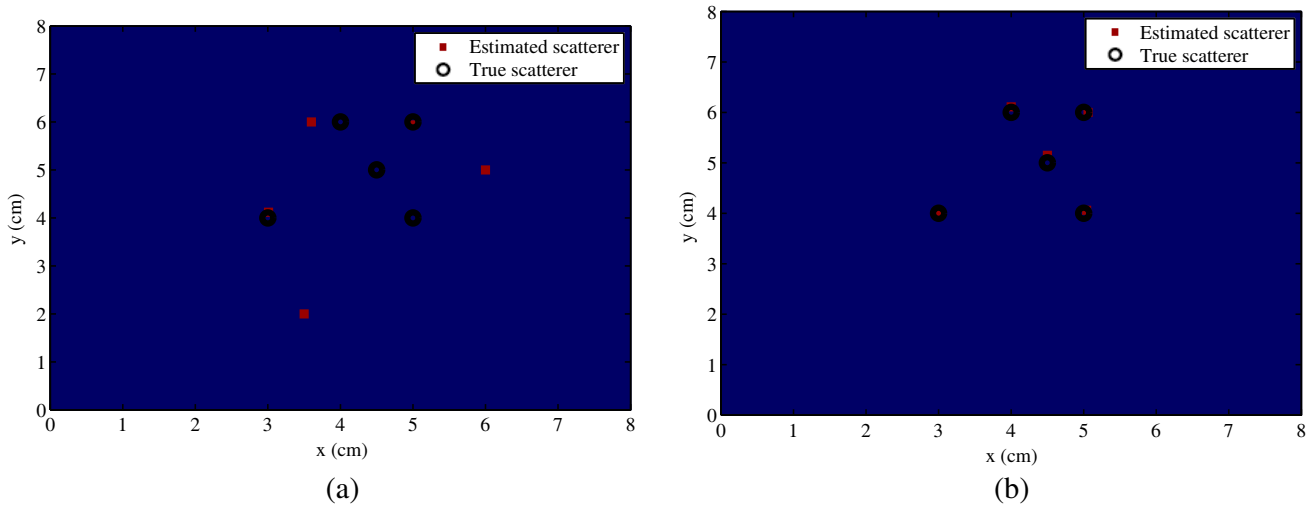

Figure 5. Imaging performance of off-the-grid scatterers, undersampling with $M = N = 50$: (a) OMP (Error 0.1672), (b) proposed algorithm (Error 0.0204).

times of theoretical resolution.are selected to guarantee the good performance by FT-based method in Fig. 6(a), and the current estimation error under the full data set (i.e., $M = N = 100$) is taken as a baseline. Fig. 6(a) compares the performance of the proposed algorithm with respect to number of sampling points. Obviously, when M, N are too small, such as $M = N = 10$, the performance by the proposed algorithm yields a very bad estimation, where the error is infinitely great. The turning happens at around $M = N = 25$, and then the performance of the proposed algorithm is improved as M, N increase. When M, N become greater than 40, one can see that the proposed algorithm outperforms FT. It accounts for the setting of M and N in previous Figs. 2–4. Then, the performance of those two fixed scatterers by the proposed algorithm with different numbers of samples is tested. To make a consistency, here M and N still take their values as 50. Compared with FT, the proposed algorithm is shown to provide a good performance with far lower number of samples. In Fig. 6(b), we take the x-dimensional distance between two scatterers as the index to investigate the resolving performance by two ways. It obviously shows that except the number of samples, with the same system parameters

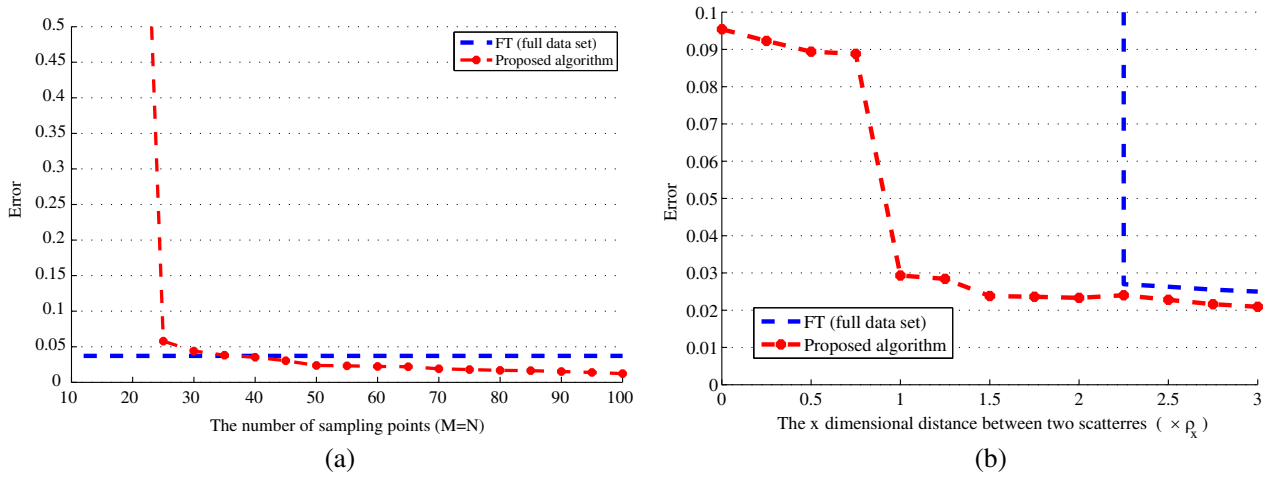

Figure 6. Imaging performance: (a) versus the varying number of samples, (b) versus the varying x-dimensional distance between two scatterers ($M = N = 50$).

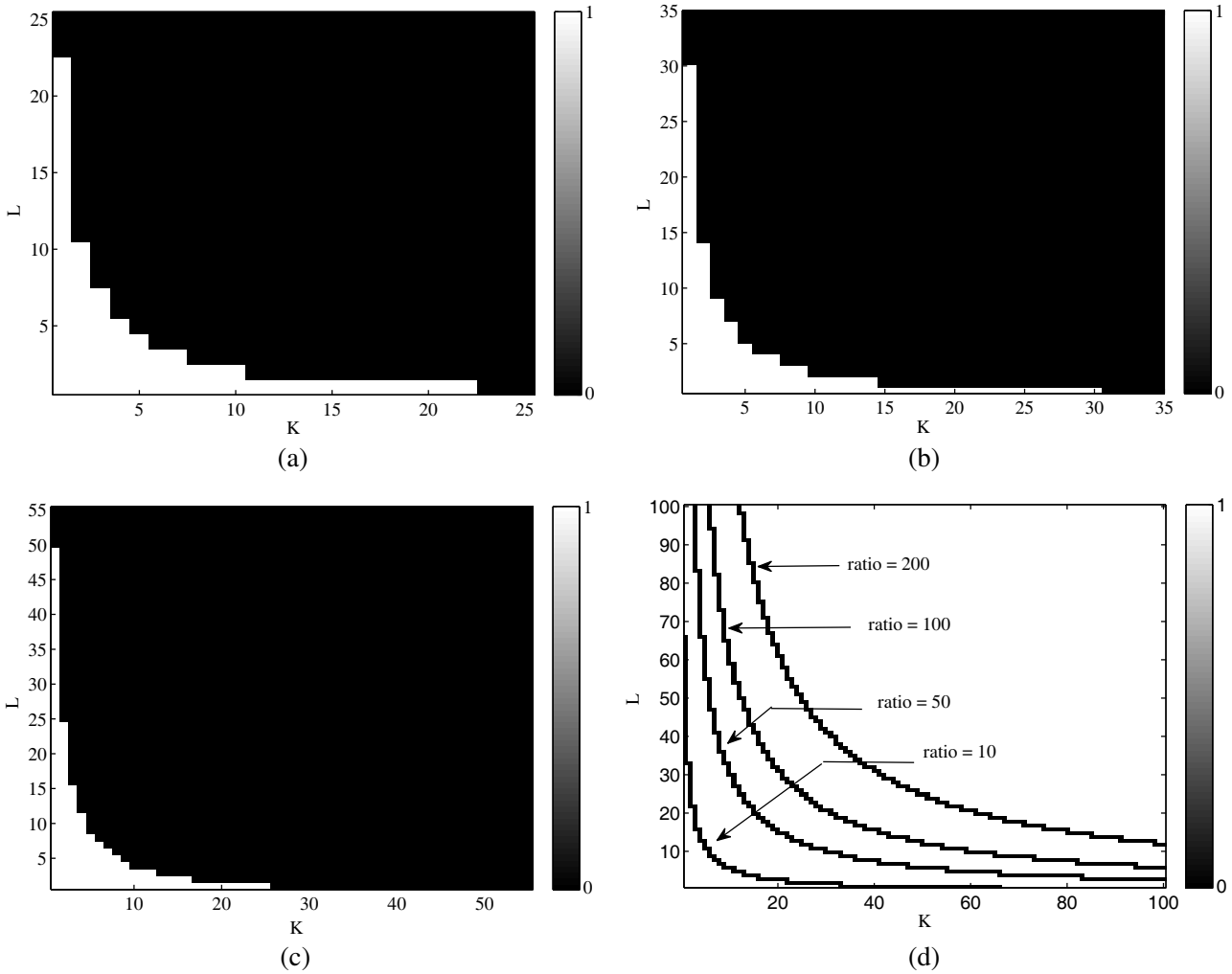

Figure 7. Computational complexity: (a) $M = N = 50$ with ratio threshold of 10, (b) $M = N = 100$ with ratio threshold of 10, (c) $M = N = 1000$ with ratio threshold of 10, (d) $M = N = 100$ with four different ratio thresholds.

setting, the resolution of the proposed algorithm is approximately better than twice that of FT.

The comparison of computational complexity between FT and our approach is conducted here. The complexity for our proposed algorithm is focused on step 2 [16], and its computational load is about

$$2KL\left(M-(K/2)\right)\left(N-(L/2)\right)+5K^3L^3 \tag{25}$$

while the 2-D FT method requires about

$$\frac{1}{2}\left(\log_2 MN\right)MN. \tag{26}$$

The ratio of the computational order of the proposed algorithm over the 2-D FT-based method is calculated numerically.

In Fig. 7, a certain value is set as a threshold of the ratio, under which the computation of the proposed algorithm is seen acceptable. Then, the ratio less than the threshold is denoted as 1, and otherwise denoted as 0. Among Figs. 7(a), (b) and (c), 10 is such a threshold, and it can be observed that with the increasing M and N (i.e., the dimensions of the data set), the range of K and L will be enlarged for acceptable complexity of the proposed algorithm. That is, the higer the number of samples is, the larger the range of K and L can be. Due to the relative small K and L compared with the size of data, it should be noted that the proposed algorithm is suitable for the scene with small size of data set. However, it is worth noting that to reduce the size of data set is the original intension of our paper, and thus our proposed algorithm is efficient and of practical application in some extent. Besides, Fig. 7(d) shows that if the requirement on the computation complexity can be relaxed, the range of K and L will increase. It means that the detection performance of our proposed algorithm can be improved.

5. CONCLUSION

This paper has proposed an improved algorithm for 2-D synthetic aperture radar imaging in the THz near field. Benefited from the matrix enhancement, the originally limited information of the target can be enhanced when given a small data set and thereby, the under-sampling scheme can be applied in practice to reduce the system complexity. By further combing the advantage of continuous parameter estimation, the proposed method can be free of grid dependence and needs not to make the interested scene pre-discretized into finite grids. Therefore, it is able to provide high-resolution imaging performance at the case of under-sampling. The proposed algorithm has been demonstrated to outperform the traditional FT-based algorithm with much fewer measurements and shows its feasibility in applications of THz imaging.

ACKNOWLEDGMENT

This work was supported in part by the National Program on Key Basic Research Project of China (973 Program) (2014CB339806), the Major National Development Project of Scientific Instrument and Equipment (2012YQ15009205), National Natural Science Foundation of China (61605113), the Natural Science Foundation of Shanghai (16ZR1423100), the Foundation for the Youth of Colleges and Universities of Shanghai (ZZsl15009), Shanghai leading talent (2016-019), and Young Yangtse Rive Scholar.

REFERENCES

1. Luukanen, A., R. Appleby, M. Kemp, and N. Salmon, *Millimeter-wave and Terahertz Imaging in Security Applications*, Springer, Berlin Heidelberg, 2012.
2. Prozheev, I. V., O. A. Smolyanskaya, M. V. Duka, A. A. Ezerskaya, V. V. Orlov, E. A. Strepitov, N. S. Balbekin, and M. K. Khodzitsky, "Study of penetration depth dispersion of THz radiation in human pathological tissues," *PIERS Proceedings*, 1536–1539, Guangzhou, August 25–28, 2014.
3. Sheen, D. M., D. L. Mcmakin, and T. E. Hall, "Three-dimensional millimeter-wave imaging for concealed weapon detection," *IEEE Transactions on Microwave Theory and Techniques*, Vol. 49, No. 9, 1581–1592, 2001.

4. Zhang, B., Y. Pi, and R. Min, "A near-field 3D circular SAR imaging technique based on spherical wave decomposition," *Progress In Electromagnetics Research*, Vol. 141, 327–346, 2013.
5. Ding, J., M. Kahl, O. Loffeld, and P. H. Bolivar, "THz 3-D image formation using SAR techniques: Simulation, processing and experimental results," *IEEE Transactions on Terahertz Science and Technology*, Vol. 3, No. 5, 606–616, 2013.
6. Li, S., C. Li, W. Liu, and Z. Sun, "Study of terahertz superresolution imaging scheme with real-time capability based on frequency scanning antenna," *IEEE Transactions on Terahertz Science and Technology*, Vol. 6, No. 3, 1–13, 2016.
7. Franceschini, G., et al., "Inversion of phaseless total field data using a two-step strategy based on the iterative multiscaling approach," *IEEE Transactions on Geoscience and Remote Sensing*, Vol. 44, No. 12, 3527–3539, 2006.
8. Caorsi, S., M. Donelli, A. Lommi, and A. Massa, "Location and imaging of two-dimensional scatterers by using a particle swarm algorithm," *Journal of Electromagnetic Waves and Applications*, Vol. 18, No. 4, 481–494, 2004.
9. Donelli, M., I. J. Craddock, D. Gibbins, and M. Sarafianou, "A three-dimensional time domain microwave imaging method for breast cancer detection based on an evolutionary algorithm," *Progress In Electromagnetics Research M* Vol. 18, 179–195, 2012.
10. Chi, Y., L. L. Scharf, A. Pezeshki, and A. R. Calderbank, "Sensitivity to basis mismatch in compressed sensing," *IEEE Transactions on Signal Processing*, Vol. 59, No. 5, 2182–2195, 2011.
11. Tang, G., B. N. Bhaskar, P. Shah, and B. Recht, "Compressed sensing off the grid," *IEEE Trans. Inf. Theory*, Vol. 59, No. 11, 7465–7490, 2013.
12. Wang, M., W. Yu, and R. Wang, "Azimuth multichannel SAR imaging based on compressed sensing," *Progress In Electromagnetics Research*, Vol. 141, 497–516, 2013.
13. Wei, S.-J., X.-L. Zhang, J. Shi, and G. Xiang, "Sparse reconstruction for SAR imaging based on compressed sensing," *Progress In Electromagnetics Research*, Vol. 109, 63–81, 2010.
14. Roy, R. and T. Kailath, "Esprit-estimation of signal parameters via rotational invariance techniques," *IEEE Transactions on Acoustics, Speech and Signal Processing*, Vol. 37, No. 7, 984–995, 1989.
15. Hua, Y. and T. Sarkar, "Matrix pencil method for estimating parameters of exponentially damped/undamped sinusoids in noise," *IEEE Transactions on Acoustics, Speech and Signal Processing*, Vol. 38, No. 5, 814–824, 1990.
16. Hua, Y., "Estimating two-dimensional frequencies by matrix enhancement and matrix pencil," *IEEE Transactions on Signal Processing*, Vol. 40, No. 9, 2267–2280, 1992.
17. Zhuge, X. and G. Y. Alexander, "A sparse aperture MIMO-SAR-based UWB imaging system for concealed weapon detection," *IEEE Transactions on Geoscience and Remote Sensing*, Vol. 49, No. 1, 509–518, 2011.
18. Zhuge, X. and G. Y. Alexander, "Three-dimensional near-field MIMO array imaging using range migration techniques," *IEEE Transactions on Image Processing*, Vol. 21, No. 6, 3026–3033, 2012.